inorganics

MDPI

Article

Improvement in the Electrochemical Lithium Storage Performance of MgH_2

Shuo Yang [1], Hui Wang [1,2,*], Liuzhang Ouyang [1], Jiangwen Liu [2] and Min Zhu [1,2]

[1] School of Materials Science and Engineering and Key Laboratory of Advanced Energy Storage Materials of Guangdong Province, South China University of Technology, Guangzhou 510641, China; 201520115810@mail.scut.edu.cn (S.Y.); meouyang@scut.edu.cn (L.O.); memzhu@scut.edu.cn (M.Z.)

[2] China-Australia Joint Laboratory for Energy & Environmental Material, South China University of Technology, Guangdong 510641, China; mejwliu@scut.edu.cn

* Correspondence: mehwang@scut.edu.cn

Received: 15 October 2017; Accepted: 11 December 2017; Published: 26 December 2017

Abstract: Magnesium hydride (MgH_2) exhibits great potential for hydrogen and lithium storage. In this work, MgH_2-based composites with expanded graphite (EG) and TiO_2 were prepared by a plasma-assisted milling process to improve the electrochemical performance of MgH_2. The resulting MgH_2–TiO_2–EG composites showed a remarkable increase in the initial discharge capacity and cycling capacity compared with a pure MgH_2 electrode and MgH_2–EG composite electrodes with different preparation processes. A stable discharge capacity of 305.5 mAh·g^{-1} could be achieved after 100 cycles for the 20 h-milled MgH_2–TiO_2–EG-20 h composite electrode and the reversibility of the conversion reaction of MgH_2 could be greatly enhanced. This improvement in cyclic performance is attributed mainly to the composite microstructure by the specific plasma-assisted milling process, and the additives TiO_2 and graphite that could effectively ease the volume change during the de-/lithiation process as well as inhibit the particle agglomeration.

Keywords: hydrogen storage materials; MgH_2; anode material; electrochemical performance

1. Introduction

Magnesium hydride (MgH_2) has been intensively investigated as a hydrogen and heat energy storage medium [1–4] because of its high hydrogen storage capacity (7.6 wt % 110 kg/m^3), low cost, and abundance. MgH_2 is an intrinsically ionic compound. The strong Mg–H bond determines the high hydrogen desorption enthalpy (~74 kJ/mol H_2) and the high decomposition temperature (>350 °C) of MgH_2. Additionally, MgH_2 suffers from sluggish hydrogen sorption kinetics due to the slow hydrogen diffusion in the MgH_2 lattice and poor hydrogen dissociation on the surface of Mg [5–8]. To overcome the thermodynamic and kinetic problems of MgH_2, many effective methods including nanostructuring, alloying, catalyzing, and compositing have been developed by ball milling, film deposition, and chemical synthetic processes [9–14].

In 2008, MgH_2 was first reported as a potential anode material for lithium-ion batteries (LIBs) by Y. Oumellal et al. [15] since it exhibited rather high lithium storage capacity (MgH_2 + Li ↔ Mg + LiH, ~2038 mAh·g^{-1}), low work potential (~0.5 V versus Li^+/Li), and low voltage hysteresis (<0.2 V). The last point is especially superior over other kinds of conversion reaction materials, such as metal oxides, nitrides, fluorides etc. However, the large volume expansion (>85%) during the conversion reaction of magnesium hydride with lithium resulted in fast capacity fading, which is even more severe than other conversion anode materials as the metal hydride has low conductivity and high activity in the liquid electrolyte. Since then, many efforts have been devoted to improving the electrochemical performance of MgH_2 [16–21]. As reported by S. Brutti et al. [22], the ball-milled MgH_2 sample with the addition of Super P shows a relatively high discharge capacity (~1600 mAh·g^{-1}) and coulombic

efficiency (~60%), which are mainly attributed to the reduction in crystallite size and enhancement of the electronic conductivity of MgH_2. Furthermore, the addition of metal oxides is also helpful in the conversion reaction of MgH_2 with lithium. For example, Kojima et al. [23,24] added the Nb_2O_5/Al_2O_3 into the active material MgH_2, thus enhancing the coulombic efficiency of all solid-state lithium-ion batteries. However, the improved effect in the coulombic efficiency, the reversibility of the conversion reaction, and the cycling performance of a MgH_2 anode is rather limited [25–27].

In this work, the expanded graphite (EG) and TiO_2 were milled with Mg/MgH_2 by dielectric barrier discharge plasma-assisted vibratory milling (P-milling), which is especially advantageous for the preparation of composites containing few-layered graphite [28]. The electrochemical performances of the obtained composites, MgH_2–EG and MgH_2–TiO_2–EG, were compared. Additionally, the new electrode preparation method was also developed to improve the performances of hydride anodes. It was demonstrated that the reversibility of the conversion reaction and the cyclic stability of a MgH_2 anode could be greatly enhanced.

2. Results and Discussion

The MgH_2–EG composite was prepared by the hydrgogenation treatment of the milled mixture (denoted as Mg–EG) of Mg powder and expandable graphite. Figure 1a shows the XRD patterns of the as-milled and hydrogenated Mg–EG composites. After milling for 10 h, the hexagonal Mg remains the major phase of the composite, and the weak MgO peak is due to the slight oxidation during sample transfer. It is stated that the weak MgF_2 diffractions indicate the reaction of Mg with the electrode bar composed of polytetrafluoroethylene, which was also reported in previous work [20]. After hydrogenation, all the Mg diffraction peaks disappear, indicating complete hydrogenation of the Mg powder. The rutile-type α-MgH_2 phase is indexed by strong and sharp diffraction peaks, implying grain growth of MgH_2 due to the hydrogenation treatment.

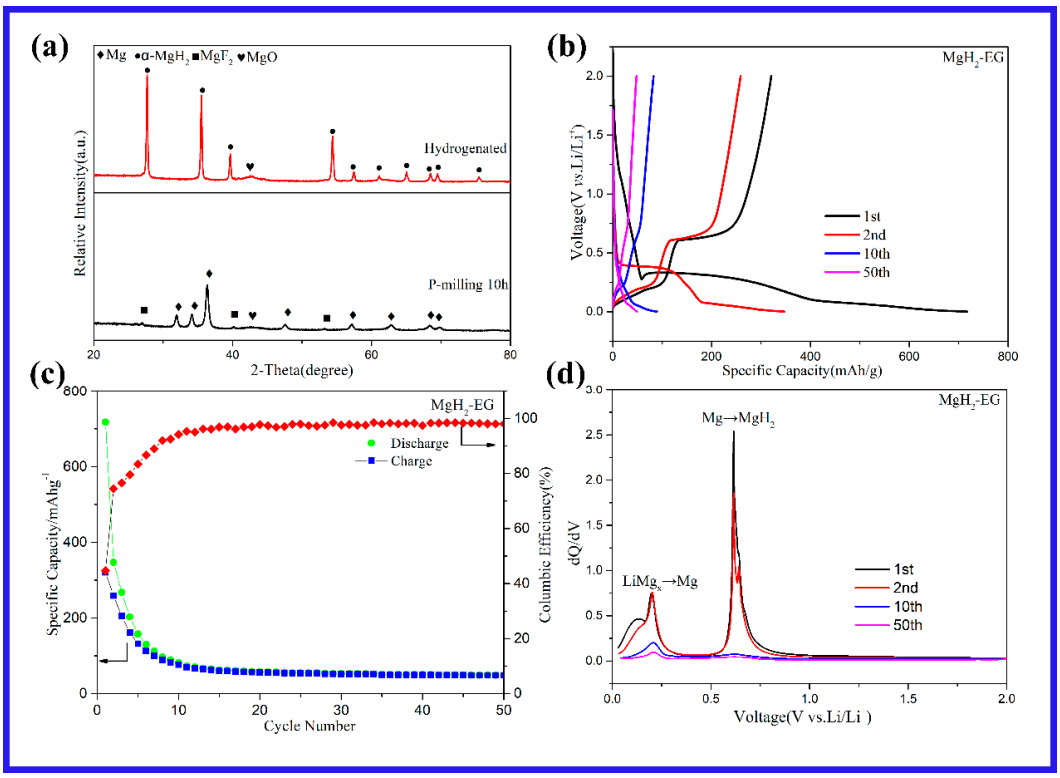

Figure 1. (**a**) XRD patterns of the as-milled and hydrogenated Mg–EG composites; (**b**) discharge/charge curves of MgH_2–EG at a current rate of 100 mA·g^{-1}; (**c**) cycling performance of MgH_2–EG electrode; (**d**) differential capacity plots (dQ/dV) of the MgH_2–EG electrode at different cycles.

Figure 1b shows the galvanostatic discharge/charge curves of the MgH_2–EG electrode at different cycles. In the first discharge profile, the potential drops rapidly from the initial open circuit potential (OCP) to 0.27 V, and then increases to 0.33 V, followed by a well-defined potential plateau assigning to the conversion reaction of MgH_2 with lithium. The slight polarization of the MgH_2–EG composite is owing to the kinetic limitation caused by the poor electronic conductivity of MgH_2 and the weak electronic contact between the active material and the nickel foam [29]. After that, the potential gradually drops further to 0.10 V with another plateau, which is attributed to the alloying of Mg with Li. Upon charging, two potential plateaus ranging from 0.10 V to 0.21 V and from 0.21 V to 0.60 V are assigned to the de-alloying reaction and the reverse conversion reaction of Mg/LiH, respectively. The first discharge capacity, amounting to 717.4 $mAh \cdot g^{-1}$, is much less than its theoretical capacity (1704.8 $mAh \cdot g^{-1}$ = 2038 $mAh \cdot g^{-1}$ × 80 wt % (MgH_2) + 372 $mAh \cdot g^{-1}$ × 20 wt % (graphite)). This result reflects the loss of active Mg during milling, as well as the kinetic limitation of coarsening the MgH_2 electrode. In addition, in the initial charge process, the MgH_2–EG electrode shows a total charge capacity of 320.6 $mAh \cdot g^{-1}$, corresponding to an initial coulombic efficiency (ICE) of 44.7%. This low ICE value also indicates the incomplete reversible formation of MgH_2 in the delithiation process.

The cycling performance of MgH_2–EG electrode is shown in Figure 1c. The rapid capacity fading in the initial several cycles may be attributed to the pulverization of active material leading to the loss of electronic contact between the active material and the nickel foam. After 50 cycles, a capacity of only 48.1 $mAh \cdot g^{-1}$ is maintained in the cell; this value is even less than the capacity (~70 $mAh \cdot g^{-1}$) contributed by the graphite component. In addition, according to the discharge profile at the 10th cycle (Figure 1b), the plateau corresponding to the conversion reaction of MgH_2 with lithium is invisible. Further, the differential capacity plots (dQ/dV) of different cycles are compared in Figure 1d. The peak centered at 0.61 V, which is assigned to the reverse conversion reaction of Mg with LiH, disappears after 10 cycles. This result further confirms the poor conversion reversibility and cycling performance of the MgH_2–EG electrode.

To improve the electrochemical performances, especially the cycling stability of a MgH_2 electrode, TiO_2 was added to the MgH_2–EG composite to accommodate the large volume variation. In addition, Mg was replaced by MgH_2 as the starting milling material in order to avoid grain growth during the hydrogenation treatment. The XRD patterns of as-milled MgH_2–TiO_2–EG composite with different milling times are shown in Figure 2a. The MgH_2 peaks for the 20 h-milled composite (denoted as MgH_2–TiO_2–EG-20 h) show a relative broadening effect compared to that of the 10 h-milled composite (denoted as MgH_2–TiO_2–EG-10 h), implying a finer grain size of the MgH_2 by longer milling time. The SEM observation shown in Figure 2c,d also displays smaller particle size (~10 μm) for the MgH_2–TiO_2–EG-20 h composite. Actually, the composite particles consist of nanosized primary particles according to the magnified SEM images (Figure 2c,d). With regard to the graphite after P-milling for 20 h, the graphite peak around 26.6° disappears in Figure 2a, implying the formation of a disordered structure of the graphite. It is believed that the graphite could be effectively exfoliated to few-layer graphene (FLG) nanosheets due to the synergic effect of the plasma heating and the impact stress from the milling balls [28,30,31]. Additionally, the hydrogen desorption kinetic curves (Figure 2b) show that both samples could release ~3.4 wt % H_2 within 15 min, corresponding to the actual MgH_2 content of ~44.3 wt % in the MgH_2–TiO_2–EG composite.

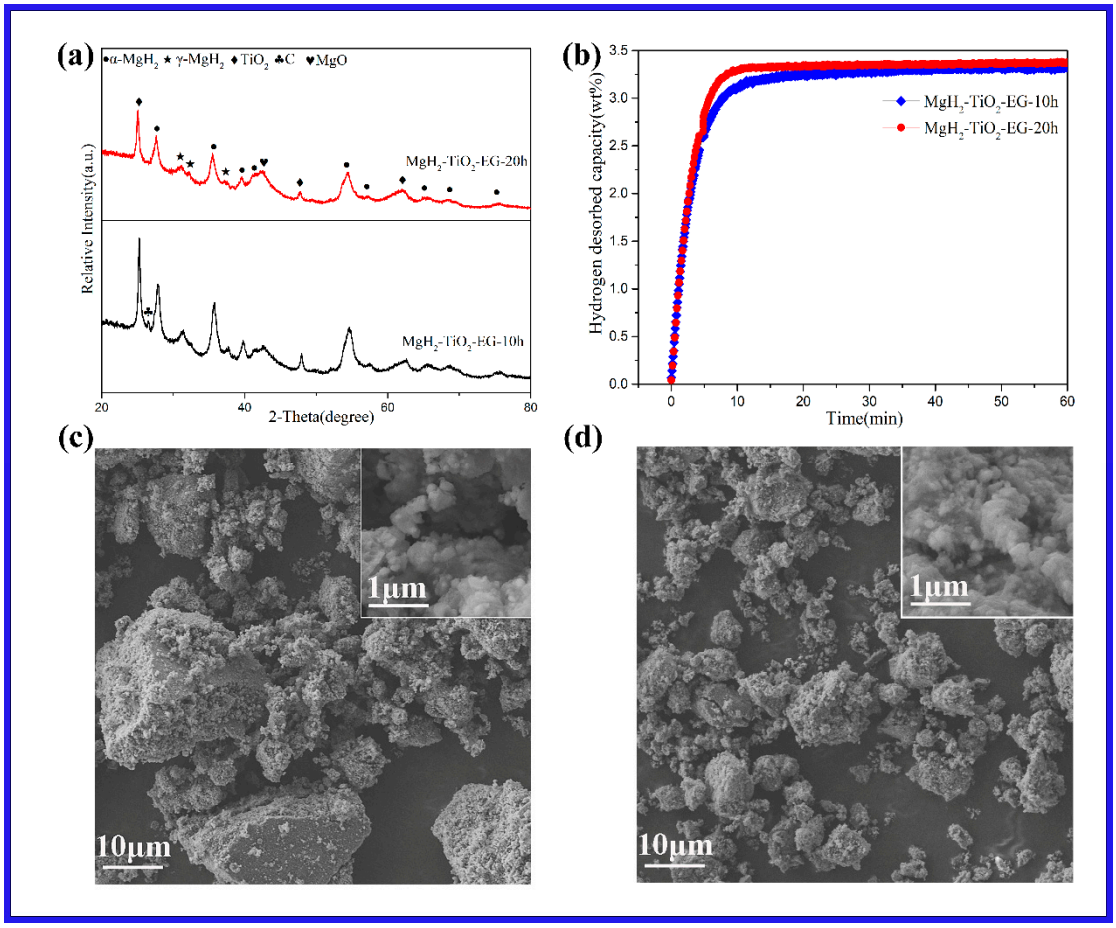

Figure 2. (**a**) XRD patterns of as-milled MgH_2–TiO_2–EG-10 h and MgH_2–TiO_2–EG-20 h composite; (**b**) desorption kinetic plots of MgH_2–TiO_2–EG-10 h and MgH_2–TiO_2–EG-20 h composite measured at 400 °C; and typical SEM images of (**c**) MgH_2–TiO_2–EG-10 h composite and (**d**) MgH_2–TiO_2–EG-20 h composite.

The galvanostatic charge/discharge curves of the MgH_2–TiO_2–EG composite with different milling times are compared in Figure 3a,b. In the first discharge profile, the MgH_2–TiO_2–EG-10 h composite electrode delivers a total discharge capacity of ~1224.6 mAh·g^{-1}, which is very close to its theoretical capacity (1193.9 mAh·g^{-1} = 2038 mAh·g^{-1} × 50 wt % (MgH_2) + 335 mAh·g^{-1} × 30 wt % (TiO_2) + 372 mAh·g^{-1} × 20 wt % (graphite)), and this result is also much higher than that of the MgH_2–EG electrode mentioned above. The ICE for the MgH_2–TiO_2–EG-10 h composite electrode is 46.4%, which is a little higher than that for the MgH_2–EG electrode. As seen in Figure 3c, the MgH_2–TiO_2–EG-10 h composite electrode exhibits a discharge capacity of 179.1 mAh·g^{-1} at the 100th cycle, with a capacity retention of 33%. Compared with the MgH_2–TiO_2–EG-10 h electrode, the MgH_2–TiO_2–EG-20 h electrode shows a similar initial discharge capacity (~1218.6 mAh·g^{-1}) and ICE (48.1%) but possessing a much higher cycling capacity of 305.4 mAh·g^{-1} after 100 cycles and a capacity retention of ~31%. As also shown in Figure 3c, while the MgH_2–TiO_2–EG-10 h composite electrode experiences rapid capacity fading within the first several cycles, the MgH_2–TiO_2–EG-20 h electrode delivers more stable capacity within 10 cycles, and it also shows higher coulombic efficiency throughout the cycling. Additionally, as shown in Figure 3d, the distinct anodic peak in the differential capacity plots (dQ/dV) at the 100th cycle clearly demonstrates the reversible formation of MgH_2, which indicates that the enhanced cyclic stability of the MgH_2–TiO_2–EG-20 h composite electrode is due to the enhanced conversion reaction reversibility of MgH_2.

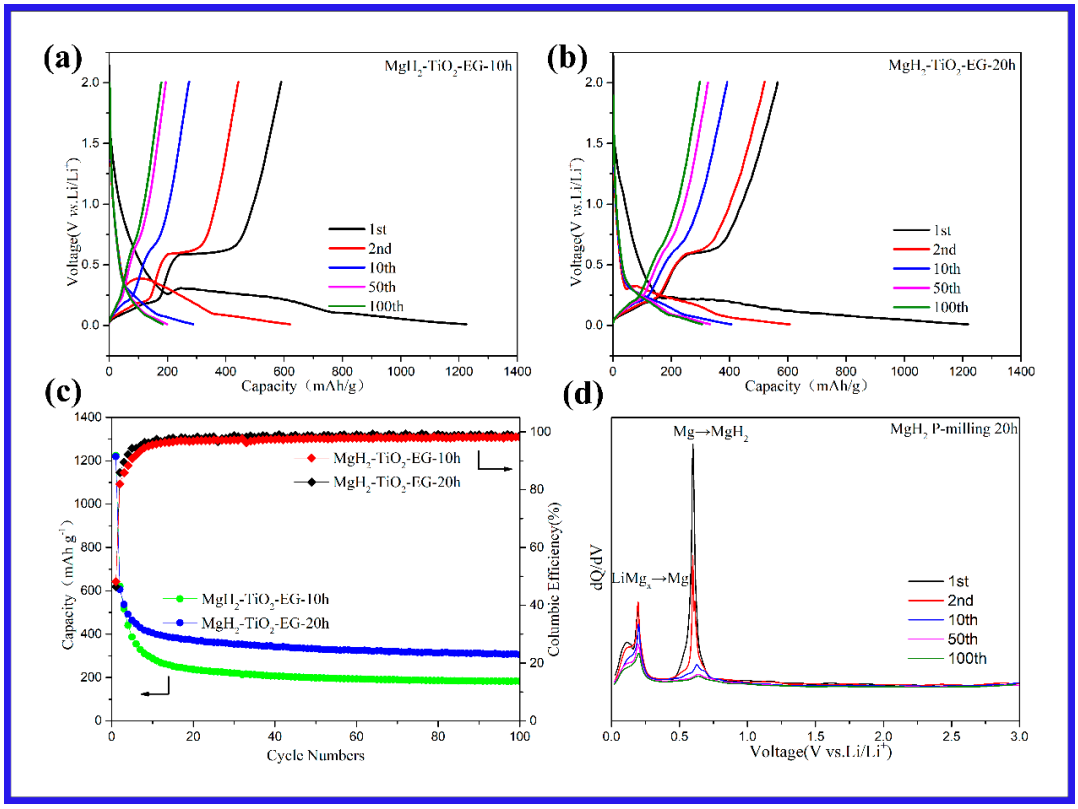

Figure 3. Discharge/charge curves of (**a**) MgH_2–TiO_2–EG-10 h and (**b**) MgH_2–TiO_2–EG-20 h electrode at a current rate of 100 mA·g^{-1}; (**c**) cycling performance of MgH_2–TiO_2–EG electrodes; (**d**) differential capacity plots (dQ/dV) of MgH_2–TiO_2–EG-20 h electrode at different cycles.

XRD analysis was performed to the change of phase structure of the MgH_2–TiO_2–EG-20 h electrode after cycling, but the result (not shown here) shows no diffractions and implies poor crystallinity of the active materials. SEM observation was also carried out to investigate the microstructural evolution of the composite electrodes, and the results are shown in Figure 4. Before cycling, the electrode surface of both the MgH_2–TiO_2–EG-10 h and the MgH_2–TiO_2–EG-20 h electrodes are composed of irregular particles with sizes less than 20 µm (Figure 4a,c), and there is no remarkable morphological difference between them. After 100 cycles, the surface morphology of both electrodes experiences obvious particle coarsening, which is due to the lithiation and delithiation of the active material, which causes repeated powder pulverization and agglomeration. This result also explains the capacity loss of the electrodes during cycling. Further, it is also shown that the particle coarsening effect for the MgH_2–TiO_2–EG-10 h electrode is more serious than for the MgH_2–TiO_2–EG-20 h electrode and the large voids between coarse particles are clearly observed. This microstructural difference indicates that large-volume changes are better accommodated by the TiO_2 and graphite additives with finer microstructure and by longer P-milling time, which help to maintain the structural integrity of the electrode.

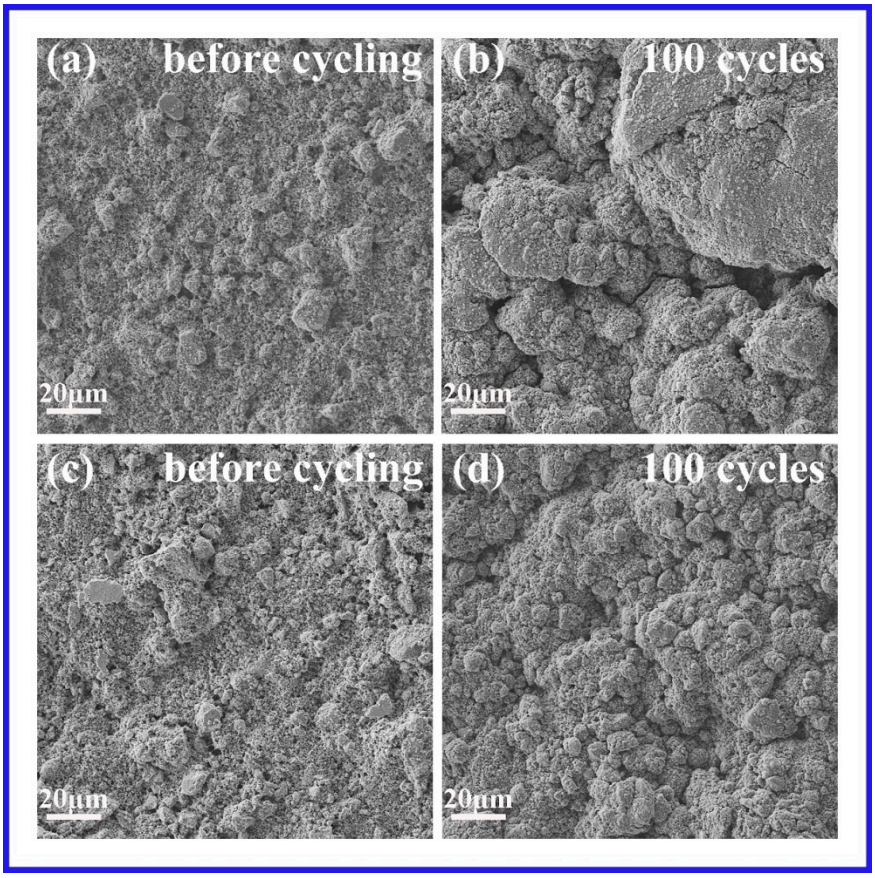

Figure 4. SEM surface morphological evolution of (**a**,**b**) the MgH_2–TiO_2–EG-10 h electrode and (**c**,**d**) the MgH_2–TiO_2–EG-20 h electrode.

3. Experimental

3.1. Materials Preparation

To synthesize the MgH_2–EG composite, 1.48 g Mg powder (99.9% purity, ~50 μm) and 0.4 g expandable graphite (EG) with a mass ratio of 80:20 were handled in a steel vial. The expandable graphite (99.9% purity, 100 mesh) was preheated at 1000 °C and held for 90 s under air atmosphere to obtain the worm-like expandable graphite. The handling process was operated in an argon-filled glovebox with an O_2 and H_2O content of less than 1 ppm to minimize the contamination. The milling was carried out on a dielectric barrier discharge plasma-assisted vibratory miller with the ball to powder weight ratio of 50:1; the details of plasma-assisted milling (P-milling) have been described in previous work [30,31]. After ball milling for 10 h, the as-prepared Mg–EG sample was hydrogenated at 450 °C under 6 MPa H_2 for 6 h.

To synthesize the MgH_2–TiO_2–EG composite, 2 g mixture of MgH_2 powder (hydrogen-storage grade), TiO_2 powder (99.0% purity, ≥325 mesh), and the worm-like EG with a weight ratio of 5:3:2 were handled in a steel vial and milled with the same parameters for 10 h and 20 h and denoted as MgH_2–TiO_2–EG-10 h and MgH_2–TiO_2–EG-20 h, respectively.

3.2. Material Characterization

X-ray diffraction (XRD, Empyrean diffractometer, PANAlytical Inc., Almelo, The Netherland) with Cu Kα radiation was used to characterize the phase structure of the samples. The microstructure was observed by using a scanning electron microscope (SEM, Carl Zeiss Supra 40, Oberkochen, Germany).

To determine the hydrogen content of the as-prepared MgH_2–TiO_2–EG sample, the desorption kinetics were measured at 400 °C using a Sievert-type automatic apparatus.

3.3. Electrochemical Measurement

The electrochemical properties of the active materials were measured using coin-type half-cells (CR2016) assembled in an Ar-filled glovebox. For preparation of the MgH_2–EG electrode, the active material was cold pressed directly on the nickel foam with the pressure of 20 MPa. For preparation of the MgH_2–TiO_2–EG electrode, the active material was first mixed with the conductive agent (Super-P) and the binder (polyvinylidene fluoride (PVdF)) in a mass ratio of 8:1:1 and then dissolved in solvent (*N*-methyl-2-pyrrolidinone (NMP)) to make a slurry with the appropriate viscosity. The slurry was then manually spread onto a Cu foil in the glovebox filled with Ar and dried in a vacuum oven at 80 °C for 12 h. The loading of the active material was ~1.0 $mg \cdot cm^{-2}$. The cell used Li foil as the counter and reference electrode and a Celgrad 2400 membrane as the separator. The electrolyte was 1 M $LiPF_6$ in ethylene carbonate and diethyl carbonate (1:1 by volume) with 10 wt % fluoroethylene carbonate (FEC).

The galvanostatic charge/discharge tests were performed in a voltage range of 0.01 V to 2.0 V (vs. Li/Li^+) at the current density of 100 $mA \cdot g^{-1}$ using a Land test system (Wuhan, China) at a constant temperature (30 °C).

4. Conclusions

In summary, the electrochemical lithium storage properties of MgH_2 were greatly improved by compositing with graphite and TiO_2 via the discharge plasma milling process. The resulting MgH_2–TiO_2–EG composites show a remarkable increase in the initial discharge capacity and cycling capacity compared to pure MgH_2 and MgH_2–EG composite electrodes with different preparation processes. The 20 h-milled MgH_2–TiO_2–EG-20 h composite delivered a stable discharge capacity of 305.5 $mAh \cdot g^{-1}$ even after 100 cycles, and the reversible conversion reaction of MgH_2 has been greatly enhanced. This work demonstrates the potential of the MgH_2–TiO_2 graphite composite by plasma-milled milling for electrochemical applications. The next goal is to obtain a higher cyclic capacity by suppressing the fast capacity fading within the initial discharge/charge cycle, and further elevate the reversible conversion reaction of MgH_2. It is also stated that the possible hydrogen release from hydride materials during discharge/charging should be avoided and given more attention.

Acknowledgments: We acknowledge financial support from the National Natural Science Foundation of China (Grant Nos. 51471070, U1601212), the Fund for Innovative Research Groups of the National Natural Science Foundation of China (Grant No. 51621001), and the Natural Science Foundation of Guangdong Province (2016A030312011).

Author Contributions: Shuo Yang: materials preparation, electrode preparation and electrochemical tests. Hui Wang: data analysis and writing of paper. Jiangwen Liu, Liuzhang Ouyang, Min Zhu: discussion on the research plan and experimental results.

Conflicts of Interest: The authors declare no conflict of interest.

References

1. Aguey-Zinsou, K.F.; Ares-Fernandez, J.R. Hydrogen in magnesium: New perspectives toward functional stores. *Energy Environ. Sci.* **2010**, *3*, 526–543. [CrossRef]
2. Wang, H.; Lin, H.J.; Cai, W.T.; Ouyang, L.Z.; Zhu, M. Tuning kinetics and thermodynamics of hydrogen storage in light metal element based systems—A review of recent progress. *J. Alloys Compd.* **2016**, *658*, 280–300. [CrossRef]
3. Mohtadi, R.; Orimo, S.I. The renaissance of hydrides as energy materials. *Nat. Rev. Mater.* **2017**, *2*, 16091–16106. [CrossRef]
4. Muthukumar, P.; Groll, M. Metal hydride based heating and cooling systems: A review. *Int. J. Hydrogen Energy* **2010**, *35*, 8816–8829. [CrossRef]

5. Lai, Q.; Paskevicius, M.; Sheppard, D.A.; Buckley, C.E.; Thornton, A.W.; Hill, M.R.; Gu, Q.; Mao, J.; Huang, Z.; Liu, H.K.; et al. Hydrogen Storage Materials for Mobile and Stationary Applications: Current State of the Art. *ChemSusChem* **2015**, *8*, 2789–2825. [CrossRef] [PubMed]
6. Møller, K.T.; Jensen, T.R.; Akiba, E.; Li, H.-W. Hydrogen—A sustainable energy carrier. *Prog. Natl. Sci. Mater. Int.* **2017**, *27*, 34–40. [CrossRef]
7. Crivello, J.C.; Dam, B.; Denys, R.V.; Dornheim, M.; Grant, D.M.; Huot, J.; Jensen, T.R.; de Jongh, P.; Latroche, M.; Milanese, C.; et al. Review of magnesium hydride-based materials: development and optimization. *Appl. Phys. A* **2016**, *122*, 97. [CrossRef]
8. He, T.; Pachfule, P.; Wu, H.; Xu, Q.; Chen, P. Hydrogen carriers. *Nat. Rev. Mater.* **2016**, *1*, 16059. [CrossRef]
9. Wang, Y.; Wang, Y.J. Recent advances in additive-enhanced magnesium hydride for hydrogen storage. *Prog. Natl. Sci. Mater. Int.* **2017**, *27*, 41–49. [CrossRef]
10. Yu, X.; Tang, Z.; Sun, D.; Ouyang, L.; Zhu, M. Recent advances and remaining challenges of nanostructured materials for hydrogen storage applications. *Prog. Mater. Sci.* **2017**, *88*, 1–48. [CrossRef]
11. Sadhasivam, T.; Kim, H.-T.; Jung, S.; Roh, S.-H.; Park, J.-H.; Jung, H.-Y. Dimensional effects of nanostructured Mg/MgH_2 for hydrogen storage applications: A review. *Renew. Sustain. Energy Rev.* **2017**, *72*, 523–534. [CrossRef]
12. Crivello, J.C.; Denys, R.V.; Dornheim, M.; Felderhoff, M.; Grant, D.M.; Huot, J.; Jensen, T.R.; de Jongh, P.; Latroche, M.; Walker, G.S.; et al. Mg-based compounds for hydrogen and energy storage. *Appl. Phys. A* **2016**, *122*, 85. [CrossRef]
13. Jia, Y.; Sun, C.; Shen, S.; Zou, J.; Mao, S.S.; Yao, X. Combination of nanosizing and interfacial effect: Future perspective for designing Mg-based nanomaterials for hydrogen storage. *Renew. Sustain. Energy Rev.* **2015**, *44*, 289–303. [CrossRef]
14. Shao, H.; Xin, G.; Zheng, J.; Li, X.; Akiba, E. Nanotechnology in Mg-based materials for hydrogen storage. *Nano Energy* **2012**, *1*, 590–601. [CrossRef]
15. Oumellal, Y.; Rougier, A.; Nazri, G.A.; Tarascon, J.M.; Aymard, L. Metal hydrides for lithium-ion batteries. *Nat. Mater.* **2008**, *7*, 916–921. [CrossRef] [PubMed]
16. Zaidi, W.; Oumellal, Y.; Bonnet, J.P.; Zhang, J.; Cuevas, F.; Latroche, M.; Bobet, J.L.; Aymard, L. Carboxymethylcellulose and carboxymethylcellulose-formate as binders in MgH_2–carbon composites negative electrode for lithium-ion batteries. *J. Power Sources* **2011**, *196*, 2854–2857. [CrossRef]
17. Oumellal, Y.; Zlotea, C.; Bastide, S.; Cachet-Vivier, C.; Leonel, E.; Sengmany, S.; Leroy, E.; Aymard, L.; Bonnet, J.P.; Latroche, M. Bottom-up preparation of MgH_2 nanoparticles with enhanced cycle life stability during electrochemical conversion in Li-ion batteries. *Nanoscale* **2014**, *6*, 14459–14466. [CrossRef] [PubMed]
18. Huang, L.; Aymard, L.; Bonnet, J.P. MgH_2–TiH_2 mixture as an anode for lithium-ion batteries: Synergic enhancement of the conversion electrode electrochemical performance. *J. Mater. Chem. A* **2015**, *3*, 15091–15096. [CrossRef]
19. Meggiolaro, D.; Gigli, G.; Paolone, A.; Reale, P.; Doublet, M.L.; Brutti, S. Origin of the Voltage Hysteresis of MgH_2 Electrodes in Lithium Batteries. *J. Phys. Chem. C* **2015**, *119*, 17044–17052. [CrossRef]
20. Li, D.X.; Zhang, T.R.; Yang, S.Q.; Tao, Z.L.; Chen, J. Ab initio investigation of structures, electronic and thermodynamic properties for Li–Mg–H ternary system. *J. Alloys Compd.* **2011**, *509*, 8228–8234. [CrossRef]
21. Meggiolaro, D.; Gigli, G.; Paolone, A.; Vitucci, F.; Brutti, S. Incorporation of Lithium by MgH_2: An Ab Initio Study. *J. Phys. Chem. C* **2013**, *117*, 22467–22477. [CrossRef]
22. Brutti, S.; Mulas, G.; Piciollo, E.; Panero, S.; Reale, P. Magnesium hydride as a high capacity negative electrode for lithium ion batteries. *J. Mater. Chem.* **2012**, *22*, 14531–14537. [CrossRef]
23. Ikeda, S.; Ichikawa, T.; Kawahito, K.; Hirabayashi, K.; Miyaoka, H.; Kojima, Y. Anode properties of magnesium hydride catalyzed with niobium oxide for an all solid-state lithium-ion battery. *Chem. Commun.* **2013**, *49*, 7174–7176. [CrossRef] [PubMed]
24. Ikeda, S.; Ichikawa, T.; Goshome, K.; Yamaguchi, S.; Miyaoka, H.; Kojima, Y. Anode properties of Al_2O_3-added MgH_2 for all-solid-state lithium-ion batteries. *J. Solid State Electrochem.* **2015**, *19*, 3639–3644. [CrossRef]
25. Brutti, S.; Meggiolaro, D.; Paolone, A.; Reale, P. Magnesium hydride as negative electrode active material in lithium cells: A review. *Mater. Today Energy* **2017**, *3*, 53–59. [CrossRef]
26. Aymard, L.; Oumellal, Y.; Bonnet, J.P. Metal hydrides: An innovative and challenging conversion reaction anode for lithium-ion batteries. *Beilstein J. Nanotechnol.* **2015**, *6*, 1821–1839. [CrossRef] [PubMed]

27. Sartori, S.; Cuevas, F.; Latroche, M. Metal hydrides used as negative electrode materials for Li-ion batteries. *Appl. Phys. Mater.* **2016**, *122*, 135. [CrossRef]
28. Liu, H.; Hu, R.Z.; Zeng, M.Q.; Liu, J.W.; Zhu, M. Enhancing the performance of Sn–C nanocomposite as lithium ion anode by discharge plasma assisted milling. *J. Mater. Chem.* **2012**, *22*, 8022–8028. [CrossRef]
29. Wang, M.; Li, X.; Gao, M.; Pan, H.; Liu, Y. A Novel synthesis of MgS and its application as electrode material for lithium-ion batteries. *J. Alloys Compd.* **2014**, *603*, 158–166. [CrossRef]
30. Wang, Y.K.; Yang, L.C.; Hu, R.Z.; Sun, W.; Liu, J.W.; Ouyang, L.Z.; Yuan, B.; Wang, H.H.; Zhu, M. A stable and high-capacity anode for lithium-ion battery: Fe_2O_3 wrapped by few layered graphene. *J. Power Sources* **2015**, *288*, 314–319. [CrossRef]
31. Sun, W.; Hu, R.Z.; Liu, H.; Zeng, M.Q.; Yang, L.C.; Wang, H.H.; Zhu, M. Embedding nano-silicon in graphene nanosheets by plasma assisted milling for high capacity anode materials in lithium ion batteries. *J. Power Sources* **2014**, *268*, 610–618. [CrossRef]